Image degradation due to various aero-optical environments

Matthew Kalensky, Jonathon Wells, Eric J. Jumper, Stanislav Gordeyev

Matthew Kalensky, Jonathon Wells, Eric J. Jumper, Stanislav Gordeyev, "Image degradation due to various aero-optical environments," Proc. SPIE 11102, Applied Optical Metrology III, 111020F (3 September 2019); doi: 10.1117/12.2528509

SPIE.

Event: SPIE Optical Engineering + Applications, 2019, San Diego, California, United States

Image Degradation Due to Various Aero-Optical Environments

Matthew Kalensky*, Jonathon Wells, Eric J. Jumper, and Stanislav Gordeyev
University of Notre Dame, Notre Dame, IN, 46556

ABSTRACT

High speed time-resolved wavefront and imaging measurements were taken synchronously in-flight through the boundary layer and the shear layer environments around the Airborne Aero-Optical Laboratory for Beam Control (AAOL-BC). Instantaneous point spread functions were generated using wavefront data which enabled a relationship between large-scale structures present in turbulent flows and resultant instantaneous image degradation to be identified. In this manner, image blurring patterns can be related to specific flow structures which begins to abridge the knowledge gap between treating quantitative wavefront properties and the resultant blurred images.

Keywords: Imaging, wavefronts, aero-optics, point spread function, flight tests

1. INTRODUCTION

The ability to conduct high-speed imaging through a variety of fluid environments is desirable. The functionality of high-resolution imaging systems is necessary for applications such as reconnaissance and acquisition, tracking, and pointing systems. Imaging from a high-speed aircraft introduces difficulties that ultimately limit the effectiveness of these systems.

Aero-optics refers to the field of studying the optical distortions imposed on a light beam, resultant from a locally varying density field. The small fluctuations of density in proximity of the beam change the index of refraction as described by the Gladstone Dale relation. Aero-optical induced distortions are resultant from either compressibility effects when speeds exceed Mach 0.2, or local changes in pressure associated with aerodynamic flow environments such as boundary layers or shear layers[1,2]. These aero-optical induced effects are different than the distortions imposed by atmospheric propagation. As a light or laser beam is transmitted through the atmosphere, the local total temperature variations are attributed with being the source of these distortions[3]. The work described here will focus solely on the aero-optical induced effects. As an initially unperturbed laser beam is projected from a source, through an aero-optical environment to a target, the imposed distortions result in a larger than diffraction limited size spot in the far-field and consequently, less intensity is focused on target. Similarly, imaging a distant object through these same distortions will degrade the resultant image quality. In general, the greater the aero-optical distortions, the more blurriness in the resultant image.

The airborne aero-optics laboratory (AAOL) was established to provide a transonic, in-flight testing platform where aero-optics experiments can be performed under real conditions[4,5]. AAOL was succeeded by the airborne aero-optics laboratory for beam control (AAOL-BC), redirecting the research emphasis towards application-inspired experiments. Recent work has both qualitatively and quantitatively described the wavefront aberrations imposed on an incoming laser source through a variety of aero-optical environments around AAOL-BC[6]. Coupling the ability to quantify aero-optical distortions using wavefront measurements with simultaneously recording high-speed images enables the deleterious nature of imaging through these flow environments to be studied. Here, instantaneous point spread functions are calculated from the resultant wavefront data and synchronously analyzed with the high-speed images to investigate the image degradation resultant from relevant flow features[7,8]. Previous work has characterized the imaging environment associated with looking through an optical turret[8,9]. For this study, in-flight imaging tests were performed looking through fundamental aerodynamic flows, namely a boundary layer and a shear layer.

Email | *mkalensk@nd.edu phone | (574) 631-8349

Applied Optical Metrology III, edited by Erik Novak, James D. Trolinger, Proc. of SPIE Vol. 11102, 111020F · © 2019 SPIE · CCC code: 0277-786X/19/$21 · doi: 10.1117/12.2528509

2. EXPERIMENTAL SETUP

AAOL-BC consists of two Falcon-10 aircrafts flying in close formation nominally 50 m apart. One of the aircrafts is retrofitted with a target board design pattern on the aircraft window. This aircraft, otherwise known as the "source aircraft," also projects a 532 nm diverging laser beam from a rectangular slit in the middle of the target board onto a custom-designed optical quality window mounted on the second aircraft. The second aircraft, known as the "laboratory" aircraft, is accommodated with an optical system to receive the incoming beam and image the target board on the adjacent, source aircraft. The window through which the laser beam is received and the target board is imaged, shown in Fig. 1, left plot, has a clear aperture of 0.3048 m in diameter, with optical quality better than $\lambda/10$. The window is mounted in an aluminum insert designed to mitigate instabilities to the attached boundary layer as fluid convects from the aircraft fuselage over the window. Wavefront and high-speed images were collected through the boundary layer of AAOL-BC at Mach numbers of 0.5, 0.6, and 0.7. In a separate experiment, the boundary layer was studied using an array of pitot rakes in the location of the optical window. The results showed that the boundary layer exhibited a slight deviation from a canonical description but was determined to be adequate for these studies. Greater detail pertaining to the quantitative boundary layer measurements can be found in Ref. [6].

A shear layer was generated over the optical window by installing a porous fence 0.35 m upstream of the acquisition window on the laboratory aircraft, as seen in Fig. 1, right plot. Previous work illustrated the utility of porous fences as a passive flow device, where a shear layer was created by slowing the flow downstream of the fence via turbulence-related total pressure losses[10]. The fence has a semi-circular shape with a radius of 0.152 m and is installed normal to the aircraft surface on a mounting bracket. The fence had a porosity coefficient of 0.4, defined as the area of open holes in the fence divided by the total fence area[6]. Wavefront and high-speed images were collected through the shear layer environment generated around AAOL-BC at Mach numbers of 0.5, 0.6, and 0.7.

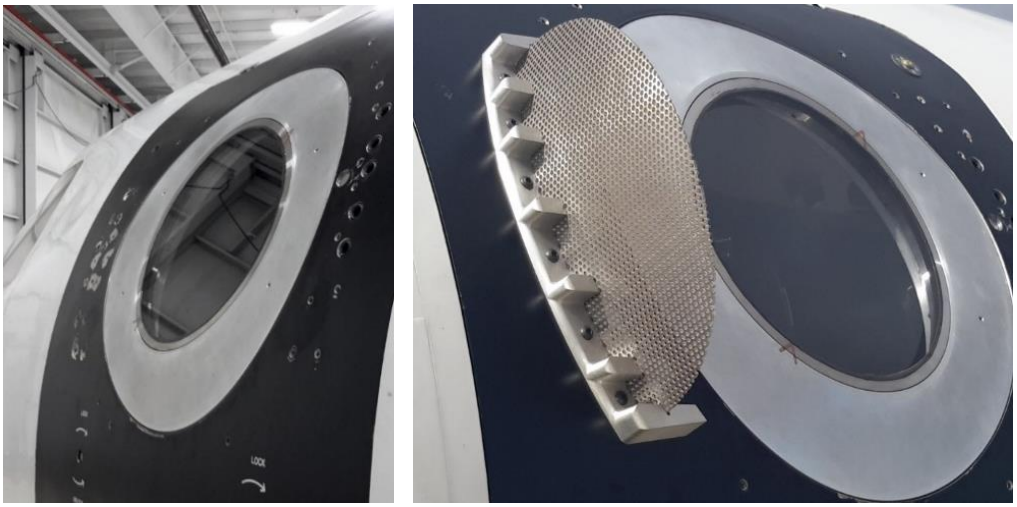

Figure 1. Left: Flat window for boundary layer tests. Right: Perforated plate installed in front of the flat window for shear layer studies

High speed imaging and instantaneous wavefronts were taken concurrently. The laboratory aircraft was equipped with a beam stabilizing system, re-imaging optical components, a high-speed Shack-Hartmann wavefront sensor (SHWFS), and a high-speed imaging camera. The optical setup is illustrated in Fig. 2. The aircrafts fly in formation with approximately 50 m separation. The source aircraft flies slightly above the laboratory aircraft such that the incoming beam is roughly normal to the flat window on the laboratory aircraft. Both the laser system on the source aircraft and the acquisition system on the laboratory aircraft utilize a tracking algorithm. The laser system must be tracking in order to aim the beam at the correct location on the adjacent plane, despite relative aircraft motion, mechanical vibration, and other system noise. The acquisition system on the laboratory aircraft uses an image based Fitts tracking algorithm to ensure the incoming beam is stabilized through the optical train and so that the high-speed camera focuses on the desired target board location on the source aircraft. The incoming beam is stabilized using a computer-controlled proportional feedback system which consists

of a tracking camera, a mirror controller, and an Aerotech gimbal with a flat mirror 0.3 m in diameter. The tracking camera on the laboratory aircraft collects images at 200 fps and computes relative image displacements in both horizontal and vertical directions. Using these computed displacements, the mirror controller commands motors on the gimbal to compensate for these angular differences.

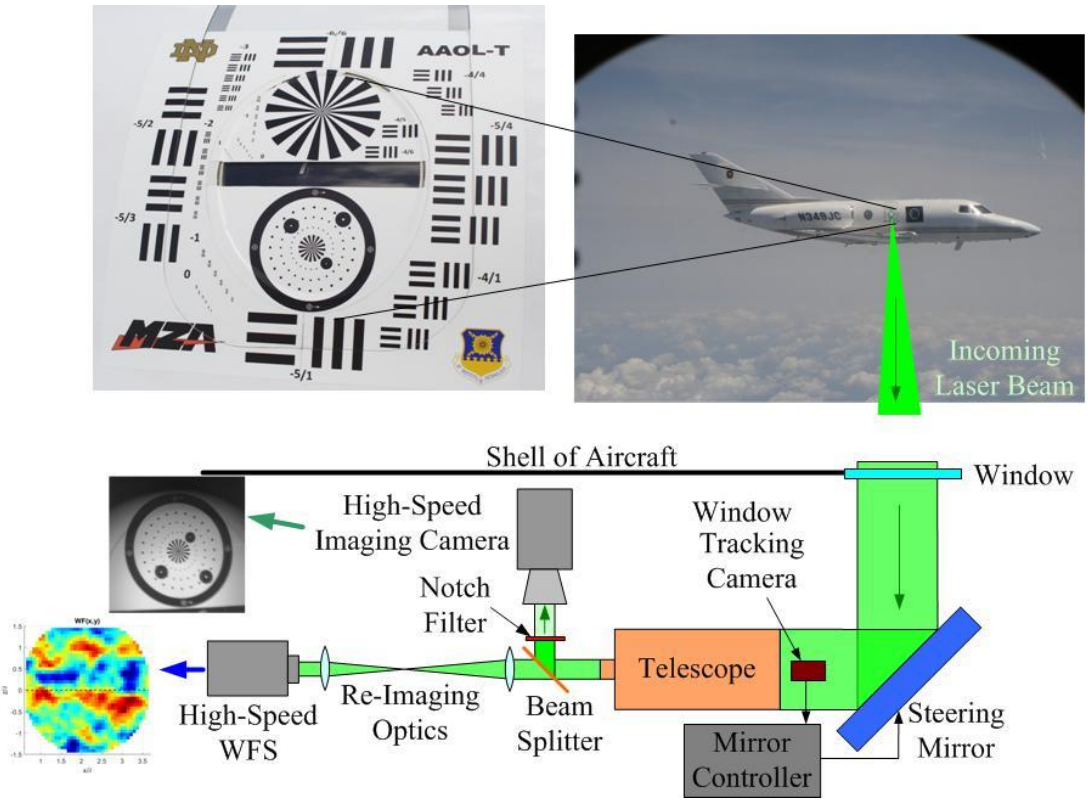

Figure 2. The optical setup and acquisition system on the AAOL-BC

After stabilization, the laser beam entered a Schmidt-Cassegrain telescope with a diameter of 203 mm, a central obscuration 64 mm in diameter (or 31% obscuration by diameter), and a focal distance of 2.035 m. A beam splitter then partitioned the received light between the SHWFS and the high-speed imaging camera. The portion of the beam directed towards the SHWFS was re-collimated using a 200 mm focal length lens and further contracted with a 250 mm and a 200 mm lens, resulting in a collimated 16 mm diameter beam entering the sensor. The SHWFS has a spatial resolution of 50x50 subapertures 0.3 mm in size, allowing the wavefront imposed on the beam to be measured with high spatial accuracy. Wavefronts were acquired at 25 kHz producing 28,000 frames per collection. For the portion of the beam directed for high-speed imaging, a dichroic notch filter was placed in front of the camera to attenuate the 532 nm wavelength. A Phantom v1840 with the pixel size of 10 microns was used as the imaging camera, coupled with a Canon MP-E 65 mm 1x magnification lens. Images were acquired at 8.1 kHz and a trigger was set between the SHWFS and the high-speed imaging camera to ensure the same initiation time for data synchronization. Flight static temperatures, pressures, and the flight Mach numbers were also recorded during the flight. Figure 3, left, illustrates the interior of the laboratory aircraft from the exit door where the optical window, seen in Fig. 1, is located. Figure 3, right, shows the rest of the laboratory aircraft configuration aft of the optical train.

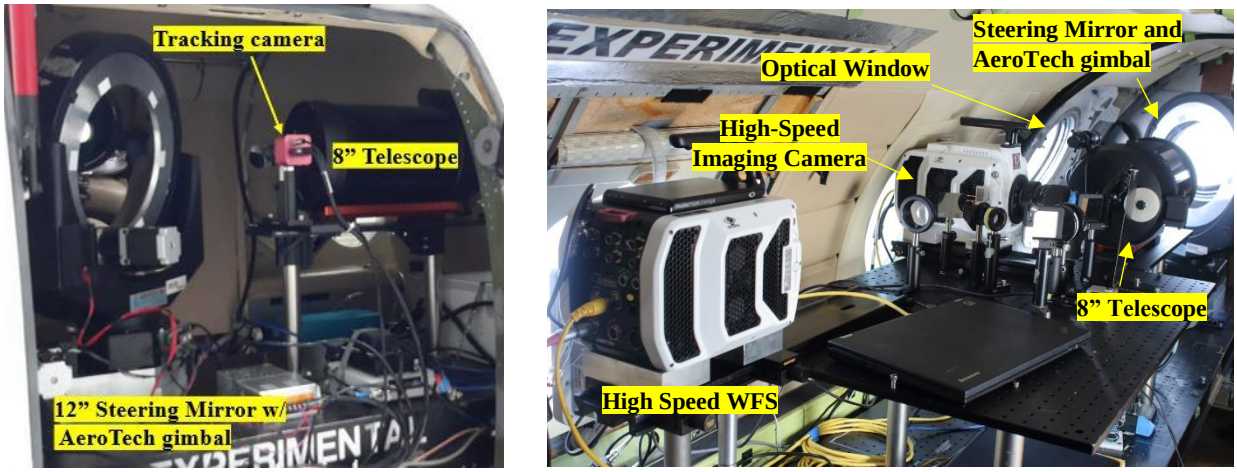

Figure 3. Interior of laboratory aircraft of AAOL-BC

The target board, imaged by the laboratory aircraft, can be seen in the top left of Fig. 2. Here, three different target designs were employed. During experiment, the target board was illuminated by the ambient sunlight. The black, horizontal and vertical rectangle patterns were designed to match the USAF-1951 target board. A spoke pattern was also implemented on the target board directly above the rectangular slit where the laser source is projected out of. The utility of this design is that the spoke pattern offers a wide range of spatial frequencies. The last design pattern implemented below the rectangular slit consists of a series of dots, decreasing in size closer to the center of the target pattern. The results discussed in this paper will primarily focus on the resultant images taken of this dot pattern design.

3. DATA ANALYSIS

Time-resolved wavefronts, W(x,y,t), were computed from the Shack-Hartmann wavefront sensor images using in-house software. Steady-lensing and instantaneous tip and tilt components were removed from every wavefront. The level of aero-optical distortions was quantified by the time-averaged spatial root-mean-square of wavefronts, denoted as OPD_{rms}, where the angular brackets denote averaging over the aperture and the overbar denotes time-averaging.

$$OPD_{rms}(t) = \sqrt{\left\langle W(x_A, y_A, t)^2 \right\rangle_{OverAperture}}, \quad OPD_{rms} = \overline{OPD_{rms}(t)}, \tag{1}$$

The point spread function (PSF) is the resultant intensity pattern if a point light source is projected into the far-field[11,12]. The experimentally measured wavefronts were also used to compute the predicted instantaneous far-field intensity patterns[8,11], i.e. PSF, as described by Eq. (2).

$$PSF(r_x, r_y, t) = \frac{\left| \int_{Aperture} \sqrt{I_0(x_A, y_A)} \exp\left[2\pi i \left\{ \frac{W(x_A, y_A, t)}{\lambda} - \frac{(x_A r_x + y_A r_y)}{R} \right\} \right] dx_A dy_A \right|^2}{\left| \int_{Aperture} \sqrt{I_0(x_A, y_A)} dx_A dy_A \right|^2}, (r_x, r_y) = \frac{2\pi R}{\lambda}(\theta_x, \theta_y) \tag{2}$$

Here I_0 is the near-field intensity (assumed to be a top-hat function), R = 101.6 mm is the aperture radius and (θ_x, θ_y) are the far-field angles. PSFs were computed via numerical integration over a discrete number of aperture points (x_A,y_A). The value of λ was chosen to be $\lambda = 0.52$ μm as a simplified approximation of the Sun's spectrum.

To quantify the properties of PSFs, spreads in both the horizontal x- and vertical y-directions were computed as,

$$\sigma_X(t) = \frac{\int_{Aperture} \left(r_x - \bar{r}_x(t)\right)^2 PSF(r_x, r_y, t) dr_x dr_y}{\int_{Aperture} PSF(r_x, r_y, t) dr_x dr_y}, \text{ where } \bar{r}_x(t) = \frac{\int_{Aperture} r_x PSF(r_x, r_y, t) dr_x dr_y}{\int_{Aperture} PSF(r_x, r_y, t) dr_x dr_y} \quad (3)$$

with a similar equation for $\sigma_Y(t)$.

Instantaneous images of the target board were recorded using a high-speed camera. An example of a collected image is shown in Fig. 4, left. Since the target board was placed over the curved aircraft window, only part of the image was in-focus. A region of the in-focus portion of the image, as indicated by a red box in Fig. 4, was extracted from every frame. This region was 50 x 100 pixels in size and consisted of two dots. The extracted image, IMAGE(*x*,*y*,*t*), was corrected for brightness and inverted such that the dots would have large positive intensity values and the background was near zero intensity. The processed image is shown in Fig. 4, right.

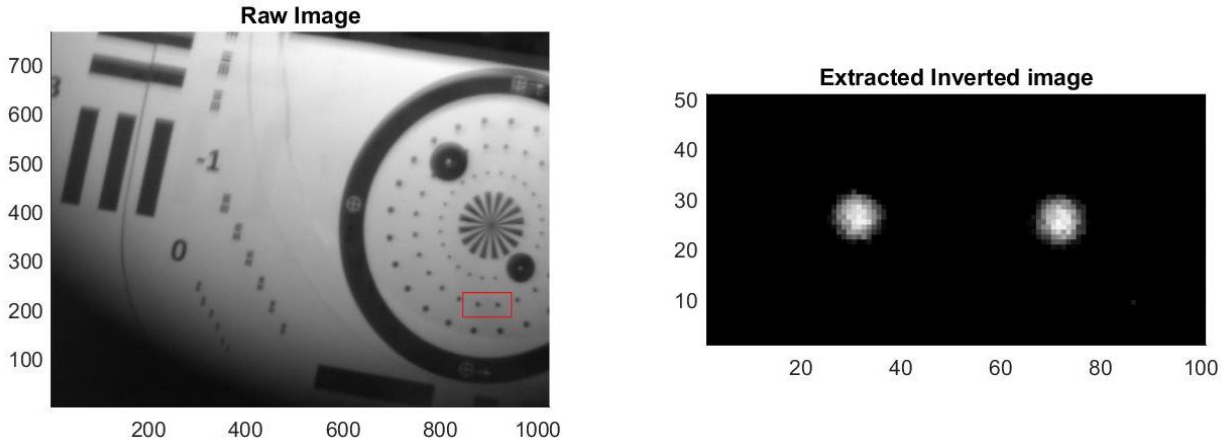

Figure 4. Left: Example of the original image, collected in flight. The region of interest is indicated by a red box. Right: Extracted and inverted region of interest used for the analysis.

Similar to the instantaneous PSF analysis, the apparent instantaneous blurring of the dots in both the x- and y-directions was quantified by the corresponding spreads of the inverted dot images as,

$$\sigma_X^{IM}(t) = \frac{\int_{AreaAroundDot} \left(x - \bar{x}\right)^2 IMAGE(x, x, t) dxdy}{\int_{AreaAroundDot} IMAGE(x, x, t) dxdy}, \text{ with } \bar{x}(t) = \frac{\int_{AreaAroundDot} x \cdot IMAGE(x, y, t) dxdy}{\int_{AreaAroundDot} IMAGE(x, y, t) dxdy}, \quad (4)$$

with a similar equation for $\sigma_Y^{IM}(t)$. The blurring in both directions was computed for the two dots and the average value was used for the analysis.

4. RESULTS

The representative wavefronts (in waves) collected through the aircraft boundary layer are presented in Fig. 5, top plots. The distortions are fairly small even at the highest taken Mach number of 0.7, with less than one wave peak-to valley. The shear layer generates a much more damaging aero-optical environment and the distortions increase with increasing Mach number. An example of representative shear layer wavefronts for M = 0.7 are provided in Fig. 5, bottom plots. Here, strong pseudo-periodic structures in the streamwise direction and elongated in the vertical direction are observed, with associated

peak-to-valley values that exceed two waves. The OPD_{RMS} values calculated for each test case are also presented in Table 1.

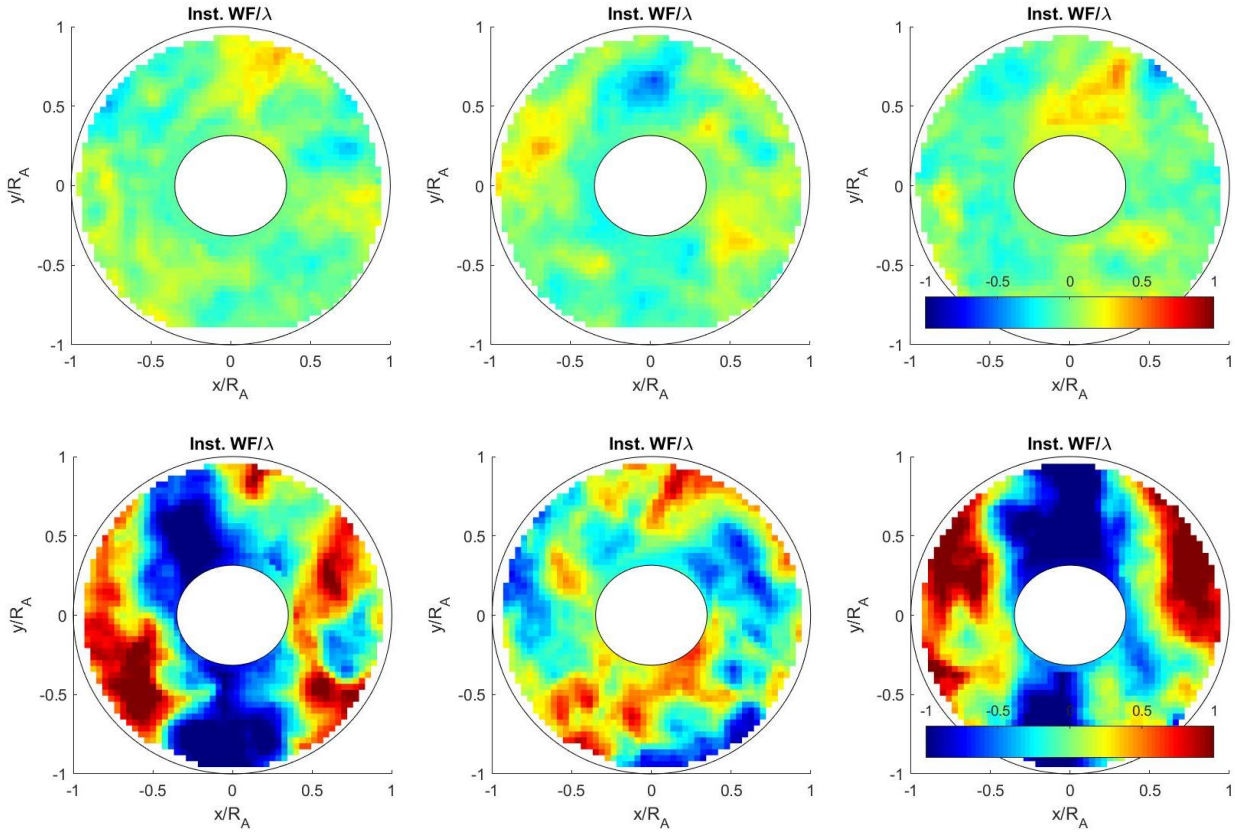

Figure 5. Representative instantaneous wavefronts, normalized by the wavelength, for the boundary layer, M = 0.7 (top plots) and the shear layer, M = 0.7 (bottom plots)

Table 1. Levels of aero-optical distortions for different flows and Mach numbers

Flow and Mach number	OPDrms (μm)	OPDrms/λ
BL, M = 0.5	0.0552	0.11
BL, M = 0.6	0.0711	0.14
BL, M = 0.7	0.0816	0.16
SL, M = 0.6	0.172	0.33
SL, M = 0.7	0.249	0.48

The shear layer cases clearly represent the scenarios of the most detrimental flow-field induced aberrations, with associated distortions of OPDrms/λ > 0.3 and significant image blurring is expected. Conversely, the boundary layer environments represent the more aero-optically benign cases in this test matrix. The boundary layer over the aircraft window creates small, less than 0.2λ distortions. In a previous paper[8], it was demonstrated that the image is essentially sharp if aero-optical distortions are sufficiently small, OPDrms/λ ≤ 0.2. Another way to demonstrate this is to compute time-averaged modulation transfer functions (MTFs) from the wavefront data. As a reminder, the MTF is the modulus of the optical

transfer function (OTF), and the OTF is the auto-correlation of the pupil function, $P(x,y,t) = \sqrt{I_0(x,y)}\exp\left[2\pi i \frac{W(x,y,t)}{\lambda}\right]$. The resultant MTFs in both the x- and y-directions for the boundary layer and the shear layer, at varying Mach numbers are shown in Fig. 6. The diffraction-limited MTF for the circular aperture with an obscuration is also presented in Fig. 6 as a dashed line for comparison. For the case of the boundary layer at M = 0.5, the MTF is close to the diffraction-limited case. Thus, the resultant images for the boundary layer M = 0.5 case are considered sufficiently sharp and are treated as approximately diffraction-limited. MTFs for the shear layer cases show significant degradation, with more distortions in the streamwise direction compared to the y-direction. This asymmetry effect will be discussed in more detail later in this paper.

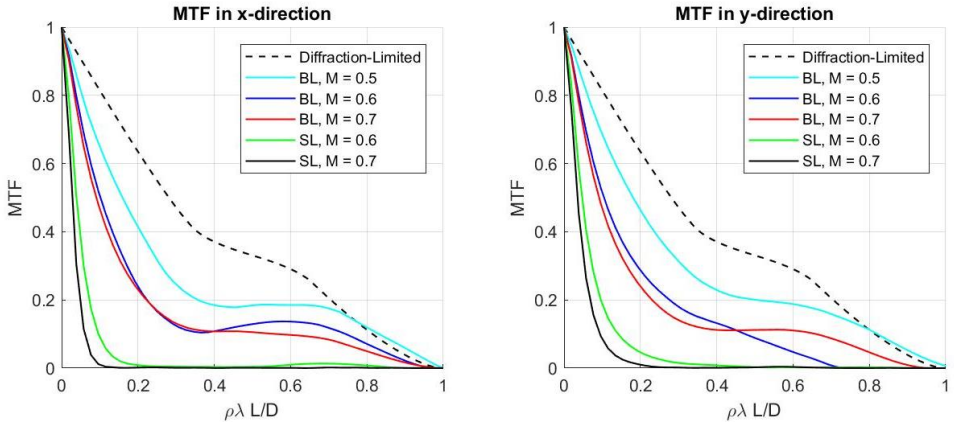

Figure 6. Time-averaged MTFs, computed from the wavefronts in x-direction (left) and y-direction (right) for both boundary and the shear layers at different Mach numbers.

In reality, non-ideal optical components, such as non-flat mirrors, off-the-shelf lenses etc., as well as averaging over finite-size pixels (the pixilation effect) will introduce additional image blurring which results in a larger dot spread in resultant images. To account for this effect, the image blurriness was quantified by the ratio of instantaneous spread, defined in Eq. (4), and the time-averaged spread due the boundary layer at M = 0.5, which can be treated as the "no-distortion case" (labelled as NoDist). This procedure was repeated for both the x and y image directions.

The results are shown in Fig. 7, where the time-dependence of the spread ratios are presented for the shear layer case of M = 0.6, Fig. 7, left, and M = 0.7, Fig. 7, right. The spread ratios were extracted from the instantaneous images, indicated by blue lines in Fig. 7, and were also estimated from the instantaneous PSF, indicated by the red lines, using Eqs. (2) and (3). Time is normalized by Λ/U_∞. For the M = 0.6 case, the experimentally-observed blurring, $\sigma^{IM}_{X,Y}(t) / \sigma^{IM}_{X,Y,NoDist}$, was approximately constant at about 2.9, and roughly the same in both directions. The average values of the predicted blurriness ratios from PSFs approximately agree with the direct measurements. Unlike the image results, the predicted blurriness ratios from PSFs show temporal variations between values of 2 and 3.5, which was not observed in the experimental results. The small difference between the image and the PSF-based spreads are expected and due to several factors. There is associated numerical error in the discrete approximation of PSFs in Eq. (2). Additionally, the reflected light from the target board is comprised of a continuous wavelength spectrum where it was only modeled as a single wavelength in the PSF calculation.

For the M = 0.7 case, the blurriness ratios in the streamwise x-direction from both the experimental and the predicted instantaneous PSF show significant temporal variations between 3 and 5, see Fig. 7, top right plot. The experimental and the predicted blurriness levels in the x-direction generally agree with each other, confirming that the aero-optical distortions are the main cause of the instantaneous image blurring. The average value of the experimentally-extracted blurriness in the vertical y-direction also agrees with the predicted PSF values, see Fig. 7 bottom right. In general, the

experimental blurriness ratios exhibit less temporal variation than those predicted by the instantaneous PSFs, similar to the M = 0.6 case, discussed above.

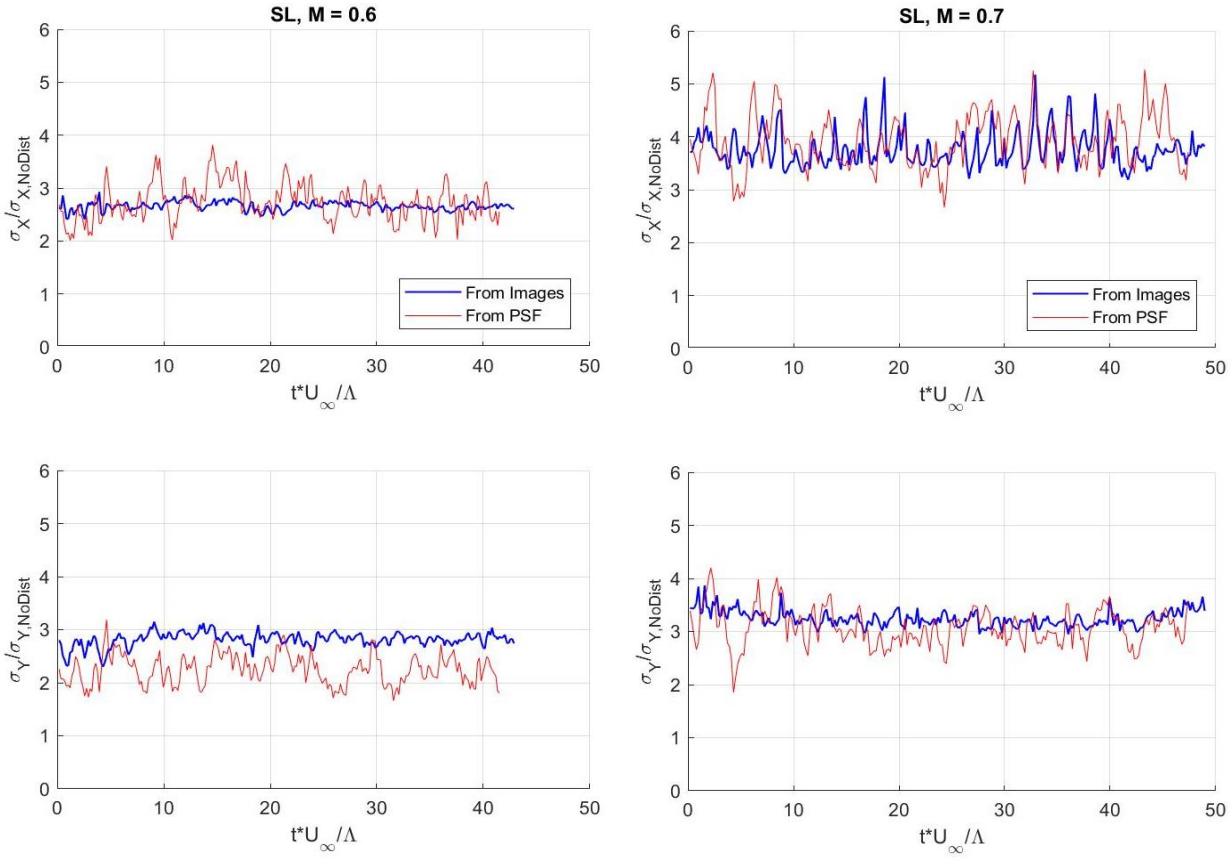

Figure 7. σ-values, normalized by the corresponding no-distortions values, σ_{NoDist}, for the shear layer case for M = 0.6 (left plot) and M = 0.7 (right plot). Direct measurements are presented by thick blue line and predicted from instantaneous PSF are shown by thin red line. Top plots are for the x-component and the bottom plots are for the y-component.

As observed in Fig. 5, bottom, the shear layer dynamics are dominated by the large, pseudo-periodic structures in the streamwise direction, which are nearly uniform in the vertical direction. As a consequence, the spatial blur in the images is larger along the streamwise x-direction; indeed, it was observed in Fig. 7, right plots. Also, the blurriness x-ratios exhibit significant pseudo-periodic variation in time, while y-ratios stay mostly constant. To further investigate which specific aero-optical features cause the largest asymmetric blurriness, the instantaneous wavefronts, corresponding PSFs, and simultaneously measured distorted dot images are presented in Fig. 8, for several consecutive times. At times tU_∞/Λ = 32.7, 33.3 and 34.5, strong vortical structures, with peak-to-valley values close to 2λ, are present in the wavefronts. The corresponding PSFs are clearly elongated in the x-direction, and the instantaneous images collected at these times also exhibit blurriness predominantly in the x-direction. In contrast, at other times, tU_∞/Λ = 33.9 and 35.1, the wavefronts are not as strong and have less spatial organization. Consequently, the resultant PSFs are approximately axisymmetric and the corresponding dot images are also blurred by the same amount in both directions. Thus, the large, spatially-organized structures present in the shear layer are the main cause of the large blurriness in the streamwise direction.

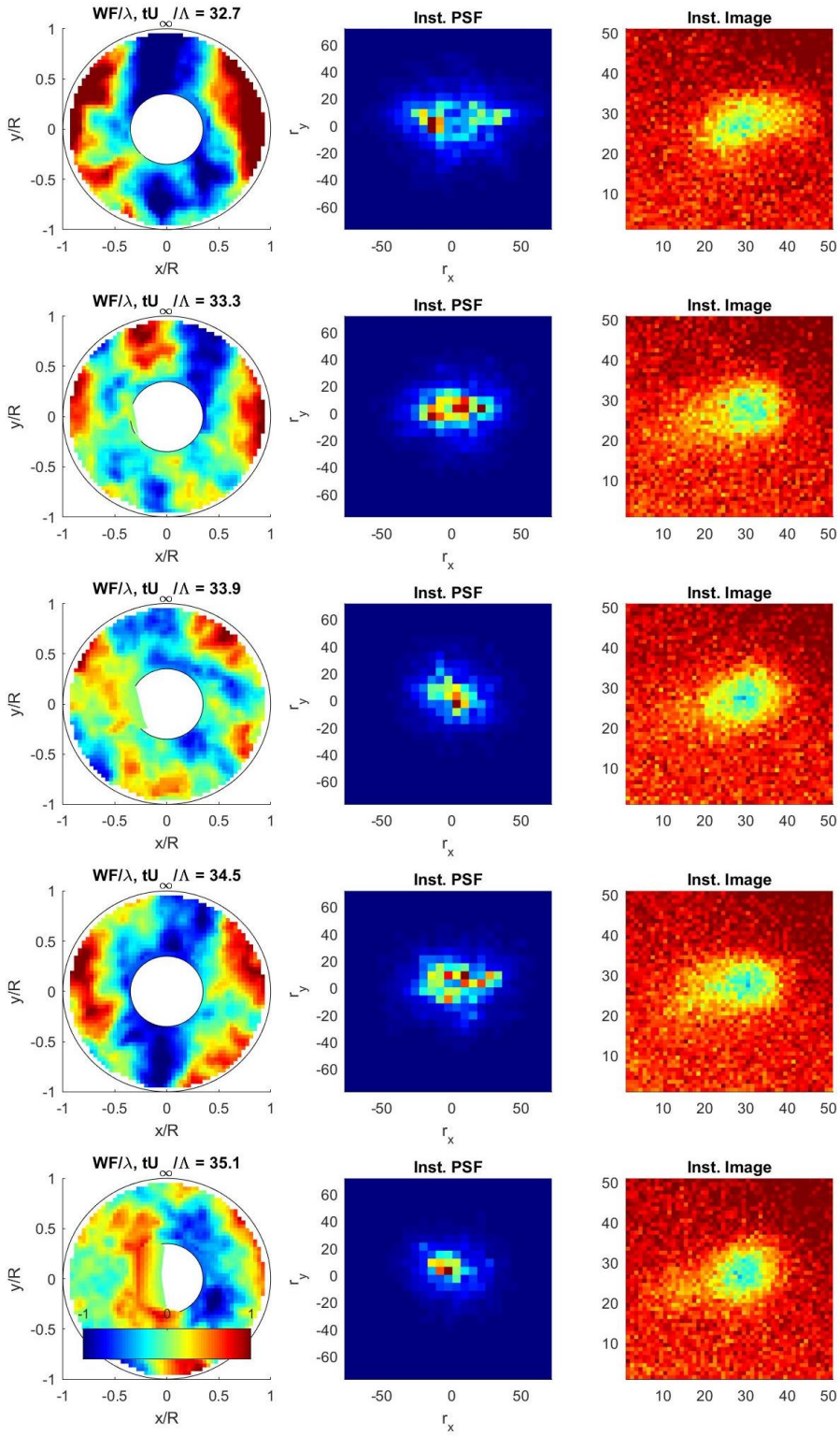

Figure 8. The instantaneous wavefronts (left column), the corresponding PSFs (middle column), and the simultaneously measured dot images (right column) for several consecutive times for the shear layer at M = 0.7.

To further confirm that the predominantly streamwise instantaneous image blurring is due to the vortical structures in the shear layer convecting over the aircraft window, the spectrum of the blurriness x-ratio for the shear layer at M = 0.7 is presented in Fig. 9. The peak in the spectrum is located at $St_\Lambda \approx 0.6$, which corresponds to the same peak, observed in the aperture-averaged wavefront spectra, also plotted in Fig. 9 for comparison. This peak is the typical passage frequency of the large-scale structures present in the shear layer, corresponding to the convective speed of the large-scale shear layer structures at approximately 0.6 of the freestream velocity[6].

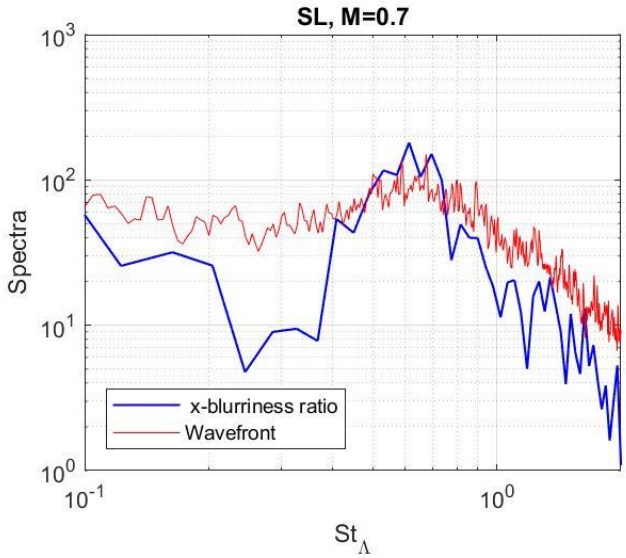

Figure 9. Power spectra of the temporal blurriness ratio in the x-direction and the aperture-averaged wavefronts for the shear layer at M = 0.7.

In Ref. [8], it was demonstrated that the time-averaged blurriness ratio is only a function of OPDrms/λ, at least for the case of separated flows over the turret. It was also pointed out that the instantaneous blurring might significantly differ from the time-averaged value. To compare the results in this paper with the results in [8], the instantaneous and time-averaged blurriness ratios in both the x- and y-directions, predicted from PSFs, are plotted in Fig. 10 versus either the instantaneous or the time-averaged values of OPDrms/λ for the shear layer, M = 0.6 and M = 0.7 cases. For M = 0.6 case, Fig. 10, left, the time-averaged blurriness ratios agree quite well with the results from [8], also plotted in Fig. 10 for comparison. Notice again that the blurriness is asymmetric with a larger degree of blurriness in the streamwise direction. The instantaneous blurriness, however, differs significantly from the time-averaged one. In addition, it does not appear to be the function of the instantaneous OPDrms(t)/λ only, with different ratios at the same OPDrms(t)/λ values. It is interesting to note that the levels of the instantaneous blurriness do not vary as much with the changes in OPDrms(t)/λ as for the time-averaged case.

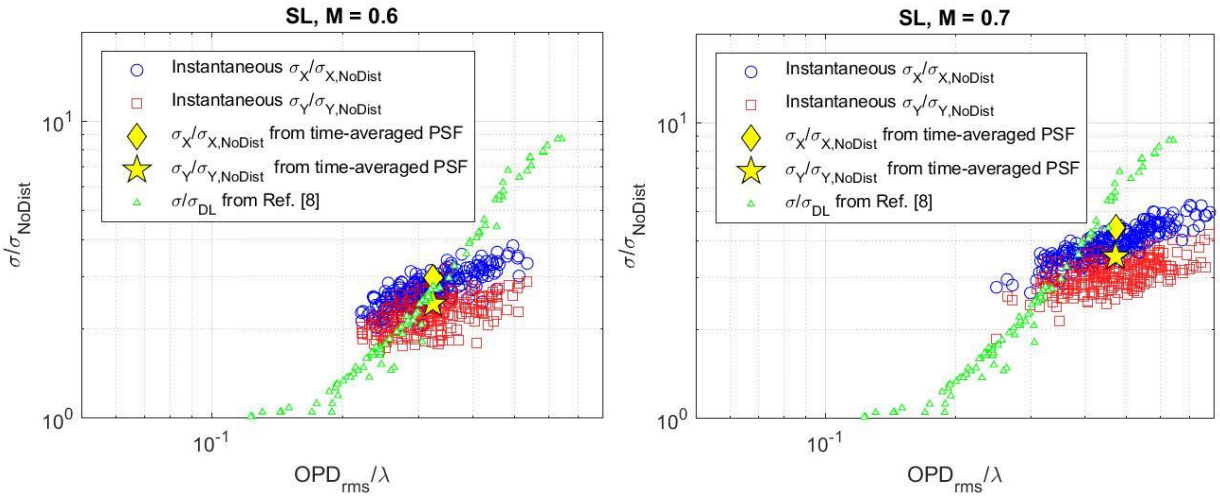

Figure 10. Both the instantaneous and the time-averaged values of the blurriness ratios as a function of the either the instantaneous or the time-averaged OPDrms/λ for the shear layer at M = 0.6 (left plot) and M = 0.7 (right plot). The time-averaged ratios as a function of the time-averaged OPDrms/λ from [8] are also presented for comparison.

For the M = 0.7 case, see Fig. 10, right, the blurriness levels were found to be less for the current studies, compared to the results in [8]. Consistent with the previous discussion, the blurriness is larger in the x-direction, compared to the one in the y-direction. The instantaneous dependence of the blurriness ratios versus OPDrms(t)/λ is very similar to the M = 0.6 case.

5. CONCLUSIONS

AAOL-BC was employed to acquire in-flight simultaneous wavefront and image data through two different aero-optical environments; a boundary layer and a shear layer. Ultimately, this allowed for relationships between relevant flow structures and consequent image blurring to be identified and further investigated. The boundary layer environment did not impose appreciable distortions on the imaging results and these scenarios were considered to be essentially diffraction limited. Conversely, the characteristic large-scale vortical structures indicative of shear layer environments did impose significant image degradation, especially in the streamwise direction. Using wavefront data, both the MTFs and PSFs for each test case were calculated and used to quantify these distortions. Furthermore, it was found that the instantaneous wavefronts, used to calculate the PSFs, can be used as a predictive approach to identify image degradation. For the Mach 0.7 shear layer test case, the simulated and experimental image blurring ratios were found to be in good agreement. This confirms that the convecting vortical shear layer large-scale structures are attributed with markedly increasing image blurring seen in the streamwise direction. Results were also compared with previous work that sought to quantify image degradation through a separated, shear-layer dominant flow downstream of the turret, and the results were found to be mostly in agreement.

ACKNOWLEDGEMENTS

This work is supported by the Joint Technology Office, Grant number FA9550-13-1-0001 and Office of Naval Research, Grant number N00014-18-1-2112. The U.S. Government is authorized to reproduce and distribute reprints for governmental purposes notwithstanding any copyright notation thereon.

REFERENCES

[1] Jumper, E.J. and Gordeyev, S., “Physics and Measurement of Aero-Optical Effects: Past and Present,” Annual Review of Fluid Mechanics, 49, 419–441 (2017).

[2] Wang, M., Mani, A. and Gordeyev, S., ”Physics and Computation of Aero-Optics," Annual Review of Fluid Mechanics, 44, 299-321 (2012).

[3] Siegenthaler, J.P., Jumper, E.J., Gordeyev, S., “Atmospheric Propagation v. Aero-Optics,” AIAA Paper 2008-1076 (2008).

[4] Jumper, E.J., Zenk, M., Gordeyev, S., Cavalieri, D., and Whiteley, M., "Airborne Aero-Optics Laboratory”, Journal of Optical Engineering, 52(7), 071408 (2013).

[5] E.J. Jumper, S. Gordeyev, D. Cavalieri, P. Rollins, M.R. Whiteley and M.J. Krizo, “Airborne Aero-Optics Laboratory - Transonic (AAOL-T)”, AIAA Paper 2015-0675 (2015).

[6] Kalensky, M., Gordeyev, S., Jumper, E.J., “In-Flight Studies of Aero-Optical Distortions Around AAOL-BC,” AIAA Aviation, Dallas, TX, June 16-21 (2019).

[7] Whiteley, M. R., and Goorskey, D.J., “Imaging performance with turret aero-optical wavefront disturbances,” Optical Engineering 52(7), 071410 (2013).

[8] Gordeyev, S., De Lucca, N., Diskin, Y., Jumper, E.J., Whiteley, M.R., “Image blurring due to turbulent wakes for airborne systems: flight tests,” SPIE Optics + Photonics 2017, 6-10 Aug, San Diego (2017).

[9] Diskin, Y., Goorskey, D., Whiteley, M.R., Drye, R., De Lucca, N., Gordeyev, S. and Jumper, E.J., “Image Blurring Due to Turbulent Wakes for Airborne Systems: Simulation and Modeling,” SPIE Optics + Photonics 2017, 6-10 Aug, San Diego (2017).

[10] Gordeyev, S., W.R. Burns, E. Jumper, S. Gogineni, M. Paul and D.J. Wittich, "Aero-Optical Mitigation of Shocks Around Turrets at Transonic Speeds Using Passive Flow Control ", AIAA Paper 2013-0717 (2013).

[11] Klein, M.V., [Optics] 1st Edition, Wiley, New York (1970).

[12] Goodman, J.W., [Introduction to Fourier Optics], McGraw-Hill (1968).

[13] Nagy J.G., Palmer, K., and Perrone, L., Numerical Algorithms 36, pp. 73-93 (2004).